We are IntechOpen, the world's leading publisher of Open Access books Built by scientists, for scientists

6,900
Open access books available

186,000
International authors and editors

200M
Downloads

Our authors are among the

154
Countries delivered to

TOP 1%
most cited scientists

12.2%
Contributors from top 500 universities

CLARIVATE ANALYTICS
BOOK CITATION INDEX
INDEXED

WEB OF SCIENCE™

Selection of our books indexed in the Book Citation Index
in Web of Science™ Core Collection (BKCI)

Interested in publishing with us?
Contact book.department@intechopen.com

CFD Applications for Predicting Flow Behavior in Advanced Gas Cooled Reactors

Donna Post Guillen and Piyush Sabharwall
Idaho National Laboratory, Idaho Falls, ID
USA

1. Introduction

Nuclear energy plays an important role as a key instrument of sustainable energy supply. The 2011 U.S. EIA Annual Energy Outlook 2011 predicts a 21% growth in total energy consumption with electricity consumption growth returning to historic levels. Nuclear power can play a vital role in significantly reducing carbon emissions in the energy sector. According to the Nuclear Energy Institute (2008), nuclear energy is the nation's largest emissions-free source of power, providing more than 20 percent of the country's electricity and accounting for nearly 70 percent of U.S. emission-free power generation in 2009. Nuclear power generation emits virtually no greenhouses gases, making it a reliable power source that can provide the necessary energy to supply our growing economy while protecting the environment and ensuring the availability of energy.

Advanced nuclear reactor concepts offer potential benefits over existing reactor designs. In this work, Computational Fluid Dynamics (CFD) is applied to improve the understanding of the complex flow behavior in proposed nuclear reactor designs, such as the Very High Temperature Reactor (VHTR) and Gas Cooled Fast Reactor (GFR). The prismatic VHTR reference design, based on the General Atomics Gas Turbine Modular Helium Reactor (GT-MHR), is illustrated in Figure 1. The power conversion system (PCS) is shown to the left of the reactor. Helium coolant flows through the annulus of the hot duct as it returns from the PCS and through the annulus of the reactor vessel wall to the upper plenum. The coolant then travels downward through the fueled portion of the reactor core and into the lower plenum. The heated coolant flows out of the lower plenum and through the center of the hot duct back to the PCS to complete the cycle. The core has an annular layout with an inner and an outer reflector as well as upper and lower reflectors (graphite blocks are shown in white in Figure 1).

The GFR system features a fast neutron spectrum, helium-cooled reactor and closed fuel cycle. It can be operated at high temperatures, has a high thermal efficiency due to the high temperature reached by the coolant, and being chemically inert by nature, the coolant does not react with the structural materials in the core. The hot gases can be coupled to a direct-cycle helium turbine for electricity generation and/or to a heat exchanger where the process heat is used to produce hydrogen via high temperature steam electrolysis (O'Brien et al. 2007). Through the combination of a fast spectrum and full recycle of actinides, the GFR minimizes the production of long-lived radioactive waste. The GFR's fast spectrum also

makes it possible to use available fissile and fertile materials (including depleted uranium) much more efficiently than thermal spectrum gas reactors with once-through fuel cycles. The direction of the coolant is opposite to that of the VHTR, i.e., coolant flows upwards as can be seen from Figure 2.

The following subsections describe the CFD analyses performed for the lower plenum flow in the VHTR and upper plenum plume interaction for the GFR.
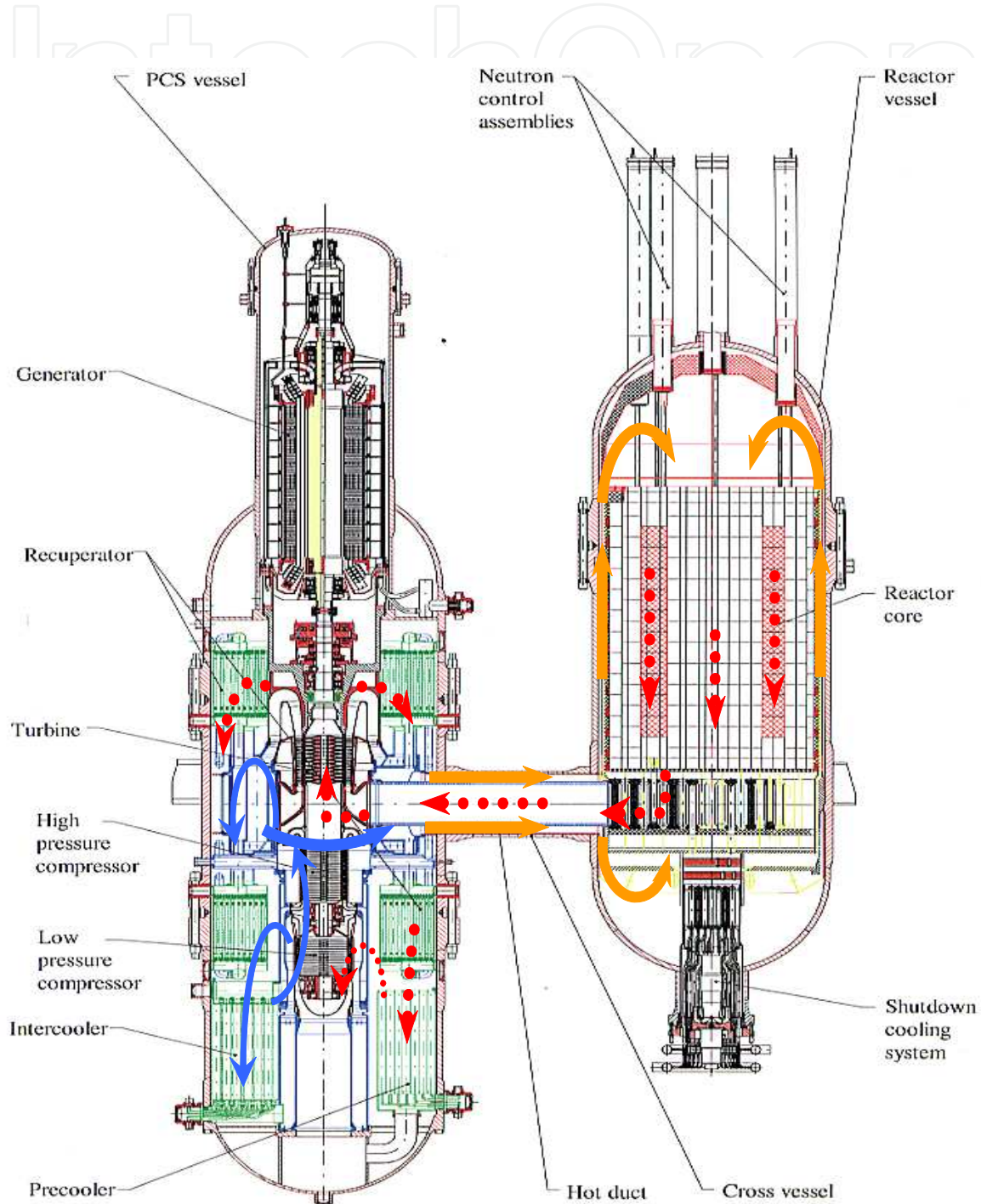

Fig. 1. Layout of the power conversion system (PCS) and reactor vessel for the gas-cooled prismatic VHTR reference design (courtesy of General Atomics)
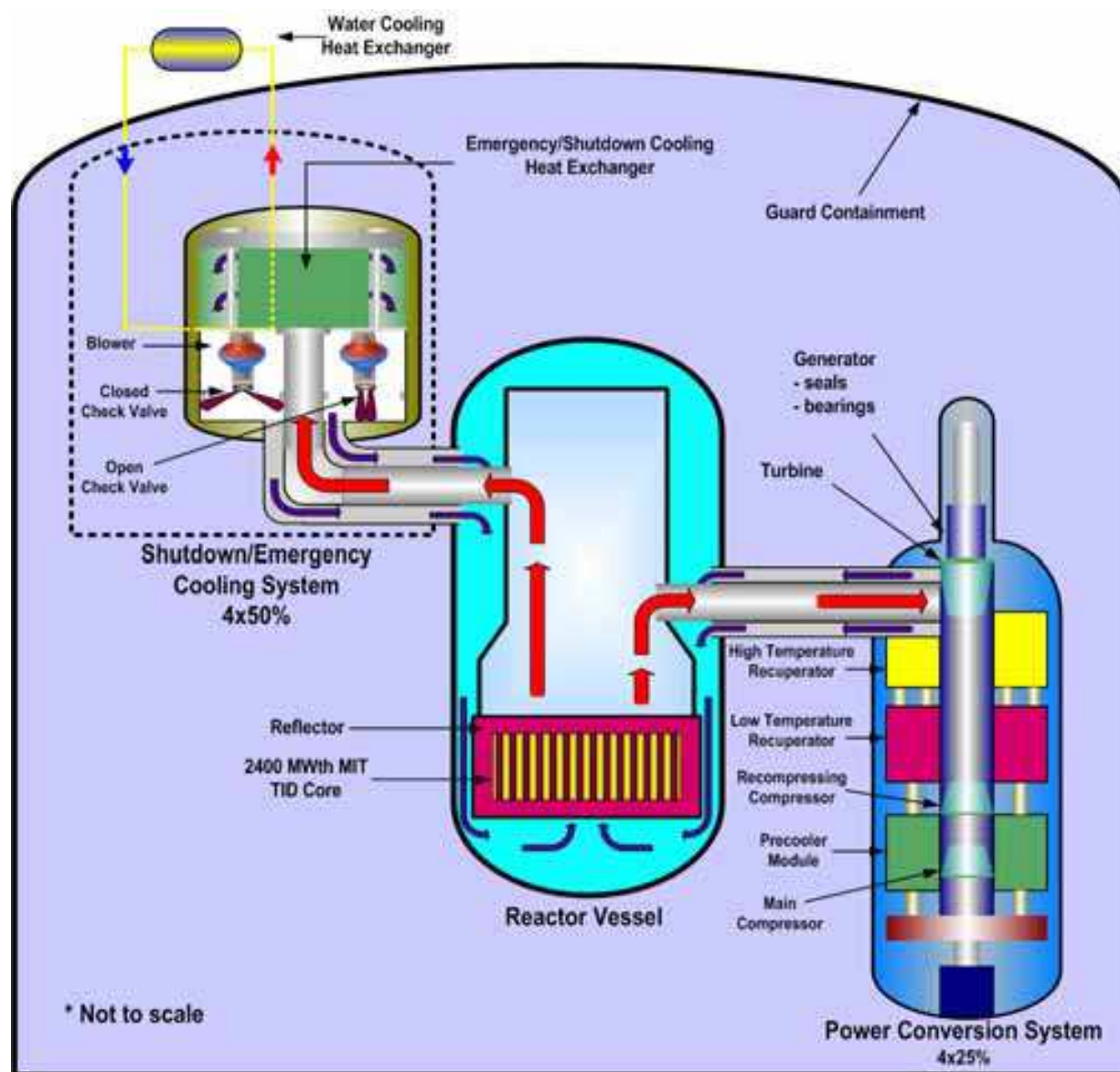
Fig. 2. Layout of the PCS and reactor vessel for the GFR (Weaver et al. 2005)

2. Very High Temperature Reactor

In the VHTR concept investigated herein, helium coolant flows vertically downward through the core and enters the lower plenum through a series of jets into a cross flow. The radial variation of the core power density creates jets of differing temperatures. Jets of hot gas discharge into the plenum, turn and flow horizontally past arrays of vertical cylindrical support posts towards the outlet duct, where the gases are fed to either a turbine or an intermediate heat exchanger for the production of electricity and/or hydrogen. Adequate mixing of the coolant flow is necessary to ensure that material structural temperature limits are not exceeded in the lower plenum or power conversion machinery.

The objective of this study is to model a section of the lower plenum of an advanced reactor concept using a commercial CFD code and compare the results to experimental data (Schultz et al. 2006).

2.1 Flow phenomena in the lower plenum of VHTR

The hundreds of coolant channels in the VHTR core combine into several dozen larger ducts just before entering the lower plenum. The lower plenum consists of a duct with structural support columns to support the graphite blocks in the core. These columns perturb the flow through the plenum. As the coolant enters the lower plenum, it turns ninety degrees to flow towards the exit duct; hence, there will be a cross-flow of coolant in the lower plenum. The cross-flow will have to negotiate the support columns and will also experience an expanding flow area on the side away from the exit duct and a converging area as it approaches the exit duct. Figure 3a illustrates a preliminary calculation of path lines of the coolant in the lower plenum colored by temperature, showing the entering jets. Figure 3b shows contours of turbulence intensity for a plan view of flow near the exit duct. The turbulence intensity is highest in the converging flow region close to the exit duct.

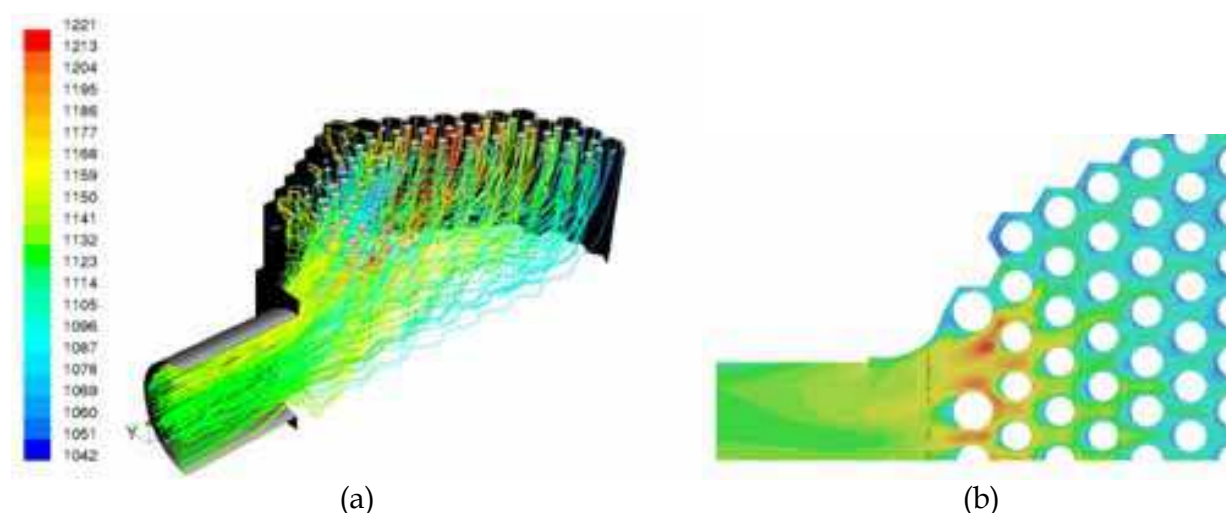(a)   (b)

Fig. 3. Flow phenomena of lower plenum showing (a) path lines of coolant in the lower plenum and (b) contours of turbulence intensity in the lower plenum in a plan view of the flow near the exit duct (Johnson 2006)

The preliminary flow calculations illustrated in Figure 3 provide insight into the flow phenomena in the lower plenum. As the flow enters the lower plenum proper, the jets will not only have some interaction with each other but also with the support columns, which are located fairly close together as shown in Figure 3b. The location of a jet will have a significant effect on its interaction with the cross-flow. Farther away from the exit duct, the cross-flow will be weaker. Hence, these jets will penetrate deeper into the lower plenum than those closer to the exit duct.

The cross-flow will have similarities to flow in tube banks. However, the flow coming straight across from the exit duct resembles flow in staggered tube banks, while flow coming from wider angles resembles flow through in-line tube banks. The flow in the lower plenum will apparently be turbulent as may be deduced from the fact that the predicted turbulence intensity is relatively large for the preliminary calculations above. The flow is expected to be unsteady due to vortex shedding behind the support columns.

2.2 Methodology

In this work, an idealized model was created to reproduce a region of the lower plenum for a simplified set of conditions that permit the flow to be treated as an isothermal,

incompressible fluid with constant properties. A scaled model of a sub-region in the lower plenum was constructed and velocity field measurements were obtained using three-dimensional Particle Image Velocimetry (PIV). Analysis of the flow by (Condie et al. 2005) was performed for the simplified case of an unheated, constant property fluid. This analysis neglects buoyancy-driven flow effects and is considered representative of normal low-power operation. These unheated flow experiments provide data for the baseline case of negligible buoyancy and constant fluid properties, which are a first step to assess the fidelity of the CFD simulations.

2.3 Experiments

Three-dimensional PIV data was obtained in the Matched-Index-of-Refraction (MIR) Facility at the Idaho National Laboratory (INL). PIV is an optical technique employed to obtain non-intrusive flow measurements. The experiments were conducted to study the turbulent flow behavior and generate data for comparison to CFD predictions. The PIV system provides both instantaneous and ensemble-averaged velocities at discrete points in the flow.

The model shown in Figure 4 models a section of vertical cylindrical support posts arranged on an equilateral triangular pitch. A symmetrical arrangement of five cylindrical columns along the model centerline and ten half-cylinders along the two parallel side walls extend the full height of the model. The model dimensions are 0.05398 m (width) x 0.558 m (length) x 0.21750 m (height). The model measures 0.05398 m in width, 0.558 m in length, and 0.21750 m in height. The ratio of the spacing between the post centerlines, L, and the post diameter, D, is L/D=2.94. The relative scale of the model to the full-scale lower plenum section is 1:6.55 (Johnson 2006).
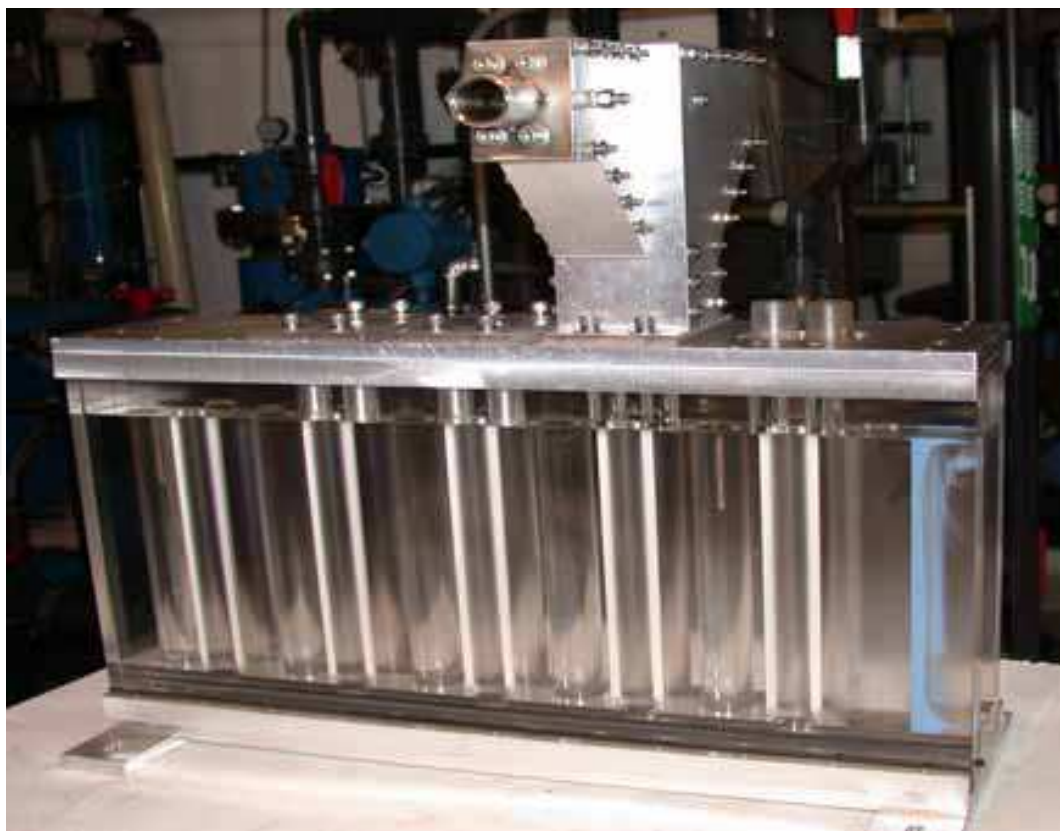

Fig. 4. MIR flow test model

The experiments, although conducted at room temperature, can be directly scaled to the prototypical system since at operational conditions the flow is momentum-dominated with negligible buoyancy and nearly constant fluid properties. Scaling studies have been performed to ensure that the flow test model with mineral oil flow under isothermal conditions duplicates the pertinent non-dimensional parameters in the lower plenum (Condie et al. 2005). The model was constructed of quartz, an optically transparent material with the same index of refraction as the mineral oil used as the working fluid of the MIR system. Seeded mineral oil with a precisely controlled temperature of 23.3 °C enters through four inlet ports above the model. The Reynolds number, based upon jet diameter and bulk flow velocity, is approximately 4300. Mineral oil from the main tunnel flows around the outside of the model at a velocity of 0.2 m/s, and mixes with the plenum flow at the model outlet.

The experiment simulates the flow in the central portion of the lower plenum, away from the outlet duct. The source of flow entering this region originates from jets exiting short coolant ducts at the corners of the hexagonal blocks, represented in the flow test model as a series of inlet jets located above the plenum. A solid wedge-shaped element at the upstream end simulates the hexagonal support block for the outer reflector and blocks cross flow from the main tunnel flow. The wedge partially blocks the inlet jet at the upstream end.

2.4 Computations

A three-dimensional computational mesh was created to replicate the geometry and dimensions of the test model. The experimental conditions were modeled using the commercial CFD code FLUENT version 6.3. In this study, the segregated solver uses a point Gauss-Seidel technique and algebraic multigrid V-cycle acceleration. The control volume technique consists of integrating the governing equations for each control volume, yielding discrete equations that conserve each quantity on a control volume basis. FLUENT stores discrete values of the conserved quantity at the cell centers and uses an upwind technique for determining face values of the conserved quantity for the convective terms. A PREssure STaggering Option (PRESTO) scheme was used as the interpolation scheme for calculating cell-face pressures. The Pressure-Implicit with Splitting of Operators (PISO) scheme, which uses a combination of continuity and momentum equations to derive an equation for pressure, was used for pressure-velocity coupling. The PISO algorithm performs both neighbor and skewness correction to decrease the number of iterations required for convergence of transient problems. The Monotone Upstream-Centered Schemes for Conservation Laws (MUSCL) scheme was used to interpolate the field variables (stored at cell centers) to the faces of the control volumes. This scheme produces a locally third-order convective discretization for unstructured meshes. The adaptive time-stepping feature invoked a time-step for the computations that varied between 0.01 and 0.02 seconds as the solution approached convergence.

FLUENT was used to solve the unsteady, Reynolds-averaged Navier-Stokes (RANS) equations for the turbulent flow present in the scaled model. RANS simulations treat the flow variables as having a time-averaged (mean) part and a turbulent part. The realizable k-ε (where k is turbulent kinetic energy [TKE] and ε is the TKE dissipation rate) turbulence modeling option with enhanced wall treatment was used. This turbulence model is known for its robustness, economy and reasonable accuracy over a wide range of turbulent flows common in industry. The entire range of turbulence scales is modeled, and only mean flow features are resolved. The enhanced wall treatment, a near-wall modeling method, combines a two-layer model with enhanced wall functions that are valid even in the wall buffer region (3 < y+ < 10). The wall

functions were developed by smoothly blending the laminar (linear) and the turbulent (logarithmic) laws-of-the-wall. The realizable k-ε model is recommended over the standard k-ε model for problems where the flow features include strong streamline curvature and vortices (Fluent 2007). The k-ε turbulence model solves for total TKE assuming turbulent viscosity is isotropic. However, the generation of TKE due to mean flow gradients may be different depending on which mean flow velocity gradients are being considered.

It is a challenge to create and execute a CFD model with a fine enough mesh to fully simulate the physical conditions in the experimental model, including the boundary layers on the walls. A grid refinement study was performed using three grids of successively varying mesh refinement. The "medium," "fine," and "super-fine" meshes shown in Figures 5a-c were generated using the Gridgen software package. The "medium" mesh was comprised of 225,243 cells, the "fine" mesh was comprised of 839,759 cells, and the "super-fine" grid was comprised of 1,265,292 cells. The unstructured grids were adapted to a polyhedral grid, which improved the speed of the calculations and yielded similar results. The "medium" polyhedral mesh was comprised of 328,816 cells, the "fine" polyhedral mesh was comprised of 689,857 cells, and the "super-fine" polyhedral mesh was comprised of 1,050,320 cells. Figure 5 shows the manner in which the adaptation procedure clustered the grid nodes in regions adjacent to solid walls (i.e., boundary layers). The goal of this study was to determine whether a k-ε turbulence model and "super-fine" grid resolution can adequately resolve the flow phenomena.

The average global cell size, h, is defined as (Celik, 2006)

$$h = \left[\frac{1}{N} \sum_{i=1}^{N} (\Delta V_i) \right]^{\frac{1}{3}}$$ (1)

Table 1 lists the average global cell size calculated using Equation 1 for the nine grids generated for this study. The volume of the fluid domain is 0.0075 m^3. The refinement factor (i.e., $h_{original}/h_{refined}$) ranges from 1.2 to 1.6.

Level of refinement	Average global cell size, h (m)	
	FLUENT grids	
	unstructured	polyhedral
medium	0.0032	0.0028
fine	0.0021	0.0022
super-fine	0.0018	0.0019

Table 1. Average global cell size for the computational meshes generated for this study

Wall boundary conditions were specified for the surfaces of the circular cylinders and half cylinders; the channel sides, top, and bottom; the hexagonal wedge; and the sides of the inlet jets. A no-slip condition was enforced at the walls. To enable specification of the flow outlet as a constant pressure outlet, the model was extended 0.3062 m beyond the physical model outlet (located at x=0.5588 m). The frictional pressure drop caused by this artificial extension is less than 8 Pa. The backflow TKE was set to 0.04 m^2/s^2, and the turbulent dissipation rate, ε, was set to 1.0 m^2/s^3. The initial conditions specified were the x-, y-, and z- components of

velocity and the static gage pressure set to zero (i.e., $V_x = V_y = V_z = P = 0$) . The working fluid in the MIR facility is mineral oil with a density of 831 kg/m³ and a dynamic viscosity of 0.0118 kg/m·s.

<div align="center">
Unstructured Grids   Polyhedral Grids
</div>

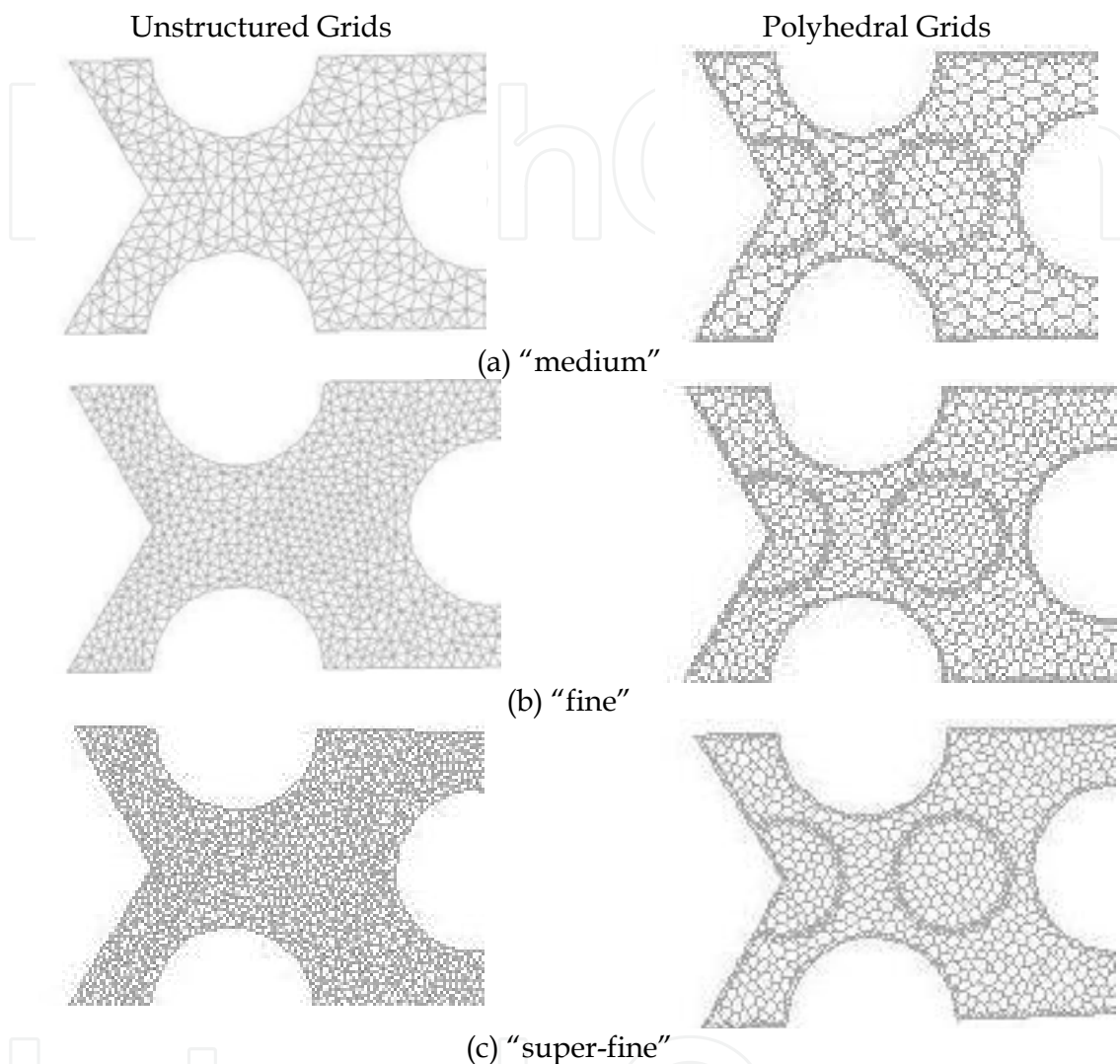(a) "medium"

(b) "fine"

(c) "super-fine"

Fig. 5. Detail sections of meshes created for grid independence study using FLUENT

Due to height restrictions in the laboratory, an elbow attached to the inlet flow conditioning block is located less than 6 inlet diameters upstream of the jet outlet into the plenum. The inlet manifold incorporates a 0.02057 m long honeycomb flow straightener, as well as two mesh screens for turbulence generation. Velocity data obtained within the jets at a location approximately 0.010 m above the plenum indicate that the flow is not fully developed, as would be expected since there is insufficient pipe length to produce fully developed flow. Also, inlet jet #1 is partially blocked by the hexagonal wedge and this flow obstruction disturbs the flow as it exits the inlet pipe.

Unfortunately, the interface between the jet outlet and the plenum was obscured due to the model construction and data could not be acquired at that location. Computations were initially run using the experimentally obtained inlet velocity profiles at a location approximately 0.01 m above the interface. Unfortunately, the PIV data point density was too

coarse to adequately resolve the inlet velocity profiles. As a result, integration of the measured velocity profiles under predicts the mass flow rate in the jets by 20 to 30%. This necessitated the application of a mass flow rate boundary condition for the CFD model, rather than the use of velocity profiles at the inlet, to ensure conservation of mass. The mass flow rate boundary condition applied at the 4 inlet jets produced a uniform velocity across the inlet jet. For jet #1, the mass flow rate was set to 0.5898 kg/s and for jets #2, #3, and #4 the mass flow rate was set to 0.8782 kg/s. A similar dilemma was encountered when examining the measured turbulent kinetic energy profiles. They were found to be too coarse and irregular. An average TKE value of 0.04 m^2/s^2 based upon the measurements was used at the inlets. In reality, the distribution of turbulence will be complex and vary across the inlet jets. The rate of turbulence dissipation is estimated at 1.0 m^2/s^3 based upon the following equation (Celik (i), 2006)

$$\varepsilon = c_\mu \frac{k^2}{\nu_t} \qquad (2)$$

where c_μ is equal to 0.09 and ν_t is the turbulent viscosity. These parameters were applied at a location approximately 0.01 m above the jet/plenum interface to avoid having to modify the existing grid.

Residuals of mass, momentum, TKE, and ε were monitored to determine iterative convergence. In FLUENT, these residuals are normalized values. The Unsteady RANS (URANS) solution was allowed to iterate until the residuals reached 1×10^{-6} for mass and momentum and 1×10^{-5} for TKE and ε. These convergence tolerances were based on previous research (Johnson 2006). The solution converged at each time step with a net difference in computed mass flux of 1×10^{-7} through the inlets and outlet.

2.5 Results and discussion

Experiments conducted at Utah State University (USU) (Smith et al. 2006) were conducted to aid in characterizing the flow regimes in an array of staggered vertical cylinders in a confined channel. A cylindrical array was designed to represent the VHTR lower plenum design and match the primary geometric dimensionless parameters of the MIR flow test model. The dimensionless cylinder pitch, P/D, equals 1.7, where P is the distance between adjacent cylinders and D is the cylinder diameter. The spanwise height to cylinder diameter ratio, H/D, equals 6.9. The USU model does not have a hexagonal wedge blocking the flow at the upstream end because the inlet is located there. Air enters through the inlet at a uniform x-velocity and flows across vertically-oriented cylinders and half-cylinders in a confined channel. The instantaneous velocity field across a centerline cylinder was measured using PIV and the resulting observations used to categorize the flow behavior into identifiable regimes (Smith et al. 2006).

For the INL MIR configuration, the maximum computed time-averaged x-velocity (Vx=1.61 m/s) is located at the bottom of the plenum, just upstream of the hexagonal wedge. The post Reynolds number at this location is 3600. The measurements obtained by the INL MIR system (for a jet Reynolds number of 4300) indicate a maximum post Reynolds number of 4450. Based upon the USU flow regime classification, the flow is expected to be turbulent outside and laminar inside the boundary layer on the posts (Smith et al. 2006).

The inlet for the USU flow configuration differs from that of the INL MIR model, where the flow enters the plenum through inlets located at the top of the model. The inlet configuration causes the flow to be highly three-dimensional for the INL MIR experiments. The downward flow from the inlets mixes with the fluid in the plenum causing the velocity to vary significantly in the y-direction, an effect that is pronounced near the inlet jets and diminishes as the flow travels downstream until it is homogeneous at the computational outlet boundary. A wake forms on the downstream side of each cylindrical support post with separation angles dependent upon flow speed (i.e., vertical location along the post). Figure 6 shows the variation in computed and measured x-velocity as a function of y-coordinate at spanwise centerline (z=0.0 m) for four x-locations (0.12022 m, 0.16850 m, 0.19807 m, and 0.26729 m). Figure 7 shows the locations of these planes relative to the model origin. The four inlet jets are depicted by the red open circles, with the jets numbered from 1 to 4 from right to left. Qualitative agreement between the experimental data is good, except for the data plane that bisects inlet jet #2. This can be attributed to the application of a mass flow rate boundary condition at the inlet jets, rather than using the actual turbulent velocity profile.

Fig. 6. Variation of x-velocity as a function of y-location in plenum

The frequency of the vortices shed from the cylindrical support posts is approximated by:

$$w_v = \frac{V_x St}{d} \qquad (3)$$

Vortex shedding occurs for $10^2 < Re_d < 10^7$, where Re_d is the post Reynolds number and the Strouhal number, St, remains approximately constant (≈ 0.2) over this range of Reynolds numbers (White, 2003). Using the maximum computed x-direction flow velocity, V_x, the

maximum vortex shedding frequency, w_v, is around 10 Hz. To capture the time progression of vortices shed from the cylinder, at least 20 data points per period should be acquired. This dictates a system response of at least 200 Hz for the data acquisition system.
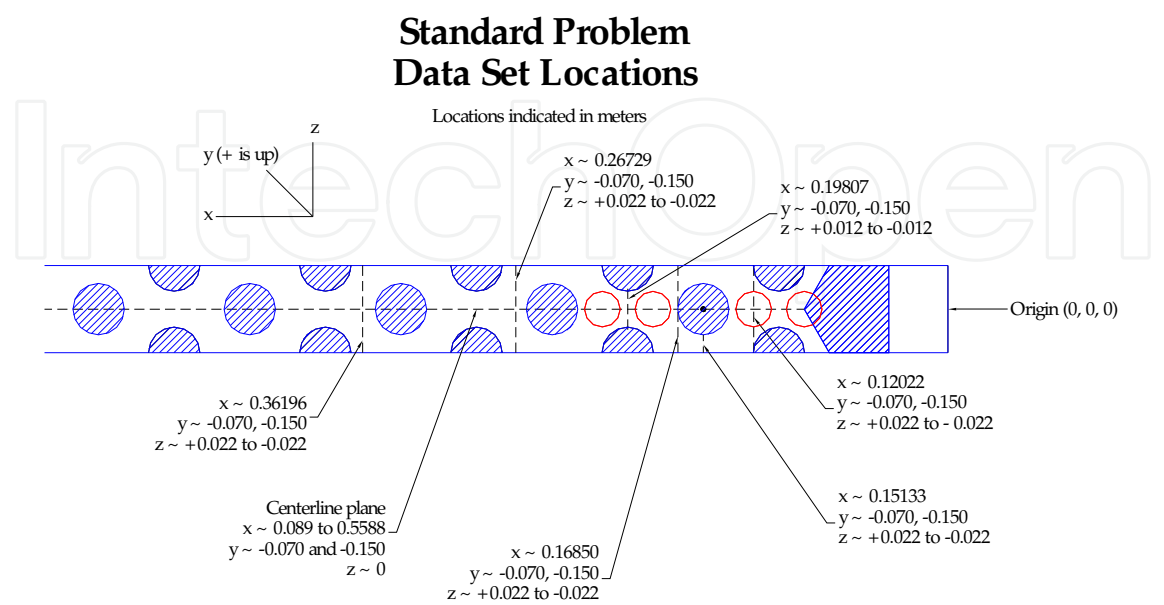

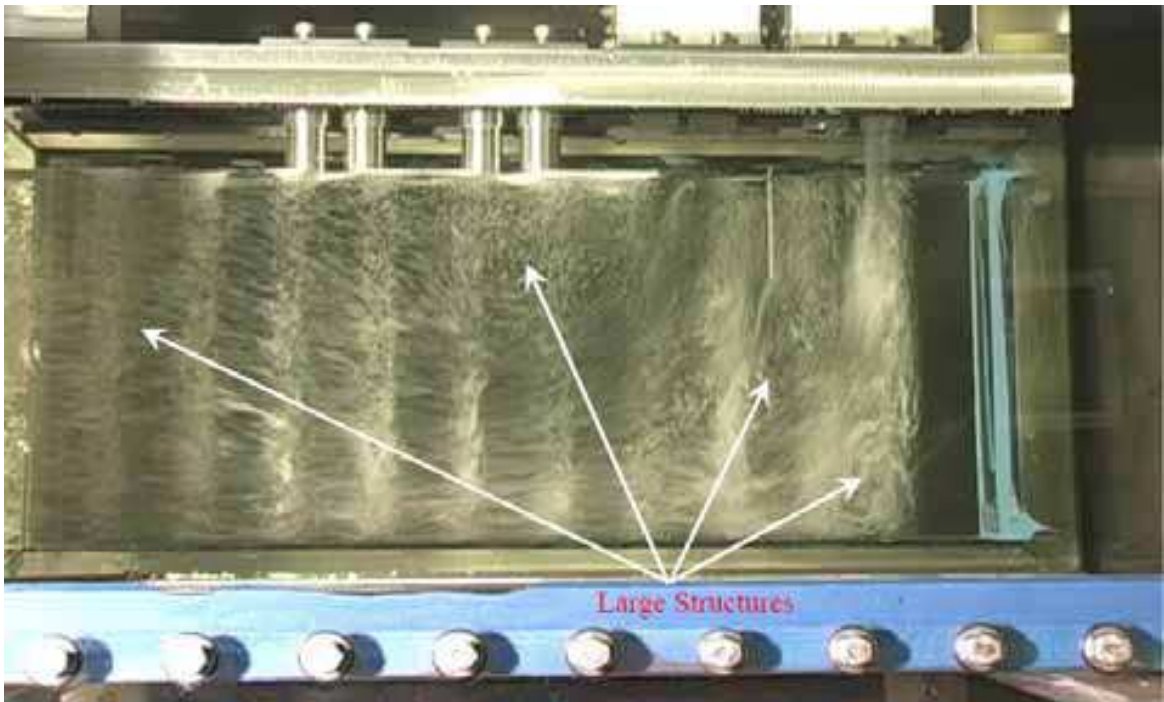Fig. 7. Data planes relative to model axis origin for data analysis

Fig. 8. Flow visualization of four jets operating at a jet Reynolds number of 4300 (McIlroy et al. 2006)

Figure 8 shows a snapshot of flow in the lower plenum model with all four jets operating (McIlroy et al. 2006). To facilitate visualization, air is injected into the flow of the rightmost jet. Air was not injected into all four jets because the resulting mass of air bubbles would

make visualization of the flow structure impossible. The bubble-laden mineral oil flows downward into the plenum and exits through the outlet on the left. Areas of flow stagnation/recirculation, as well as those with enhanced mixing, are identified. The figure shows a complicated three-dimensional flow, with four large structures. The first structure is the vortex in the bottom right corner of the model where the bottom surface of lower plenum meets the outer reflector wall. The second structure is a mixing region in the vicinity of the first centerline support post in the lower portion of the model. The third structure is a second large vertical vortex downstream of the leftmost jet in the upper third of the model, and the fourth structure is the contour of the outlet flow as it passes beneath the third structure (large vortex) and expands vertically upward to cover the entire exit area. These same structures are also observed in the computational results by examining the time-averaged x-velocity shown in Figure 9.

Since the PIV post-processing operation calculates ensemble-averaged flow quantities from the number of valid vectors identified in the instantaneous flow-field images, the CFD predictions were similarly averaged to enable a meaningful comparison with the data. Streamwise and spanwise slices located at approximately one-third and two-thirds of the depth of the model (y = −0.07 m and y= −0.15 m) were selected to compare the computed and experimentally measured mean velocity and turbulence quantities.
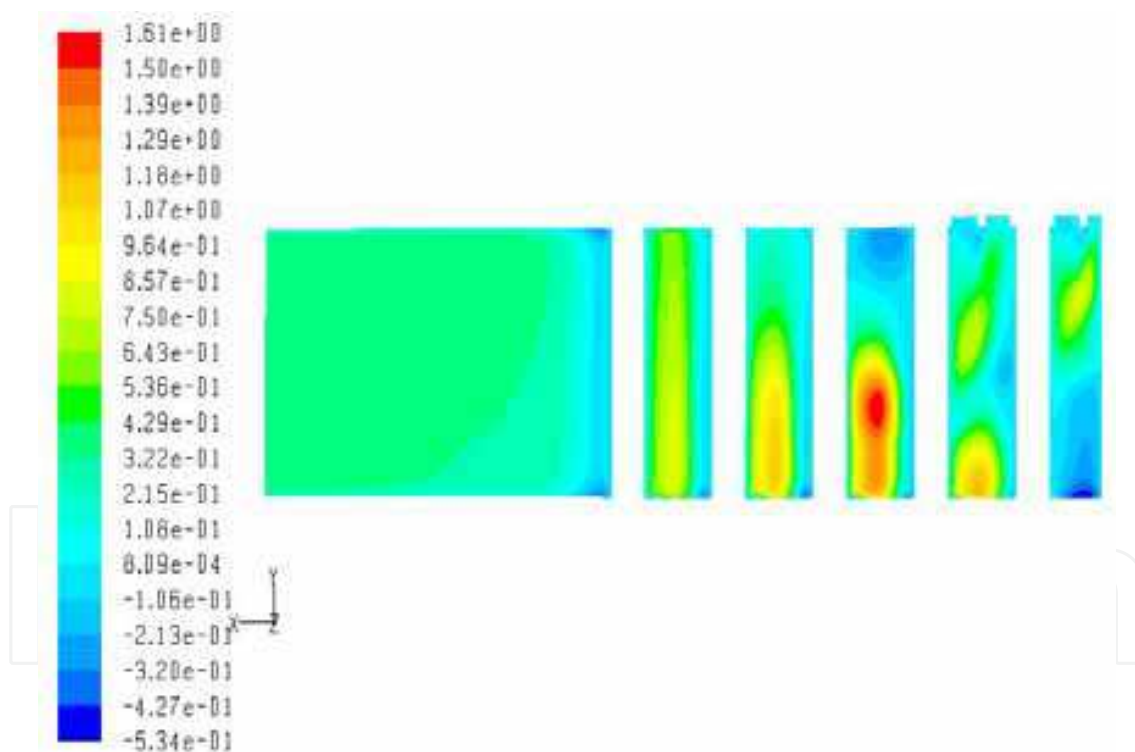
Fig. 9. Computationally-predicted recirculation zones

In FLUENT, mean statistics are collected only in interior cells and not on wall surfaces. Therefore, the plots show velocities in cells adjacent to the wall. Additionally, the velocity field measurements in this PIV data set do not adequately resolve the near-wall velocity gradients because the spatial resolution used to interrogate the raw images was designed to investigate major flow phenomena and to characterize turbulence. Consequently, the relatively large interrogation windows that were used could not accurately resolve velocity

gradients inside the boundary layers. Due to this phenomenon, the measured velocity profiles at the inlet jets could not be used as a boundary condition.

Figure 10 compares computed and measured velocities along the model centerline (z=0 m) at y-locations: −0.07 m and −0.15 m. The locations of the support posts are indicated by shaded gray bars. Experimental data is not available beyond the x=0.46 m location, because the test section supports blocked the camera views.
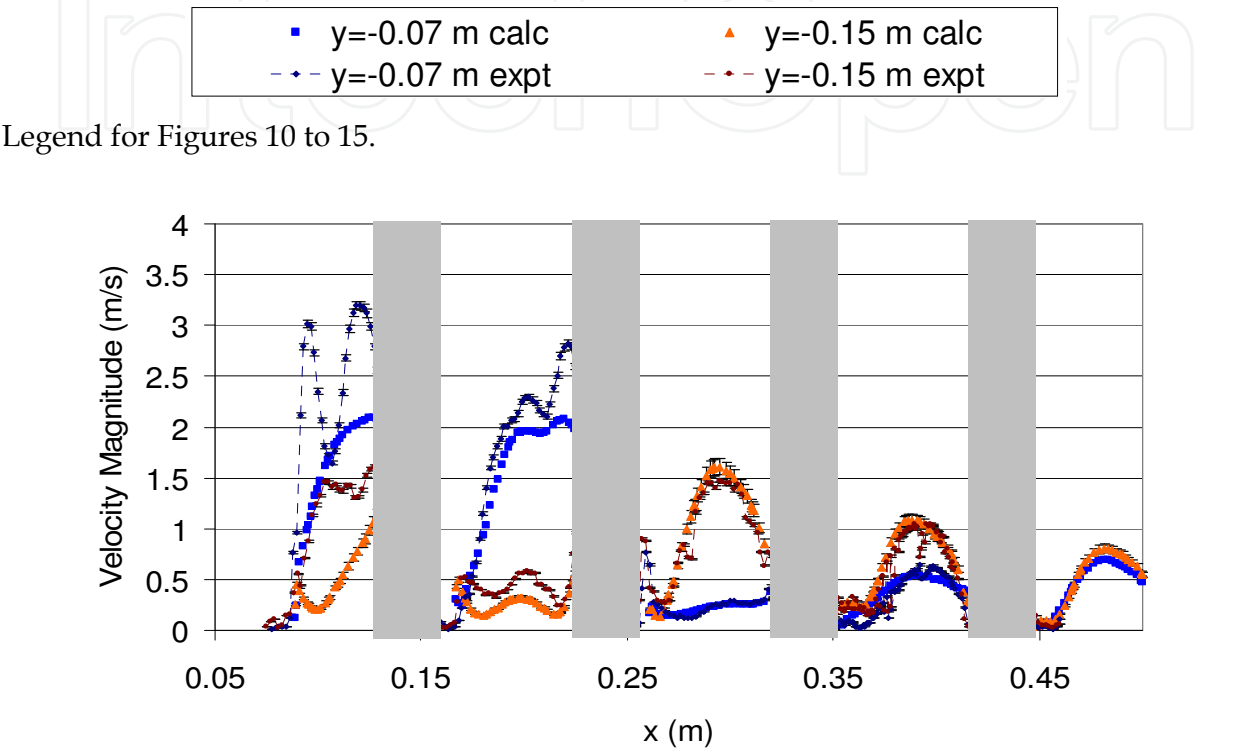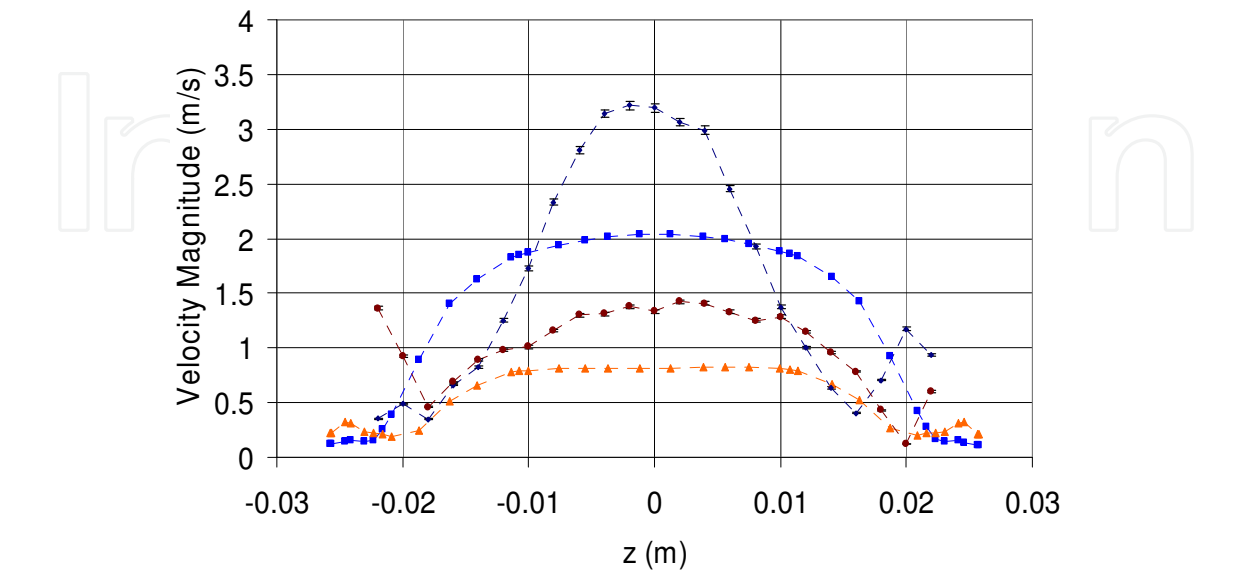

Legend for Figures 10 to 15.

Fig. 10. Velocity along the model centerline (z=0 m)

Fig. 11. Velocity on a spanwise slice (x=0.12022 m)

Figures 11 through 14 compare the computationally predicted velocities to experimental data at the following x-locations: 0.12022 m, 0.16850 m, 0.19807 m, and 0.26729 m, and y-locations: −0.07 m and −0.15 m. The largest values of velocity magnitude occur in the region below inlet jet #2. The computed long time-averaged velocity magnitudes in the region near the inlet jets differ from the measured values due to the boundary condition applied at the inlet jets. Downstream from the inlet jets, better agreement between the computed and measured values is seen.
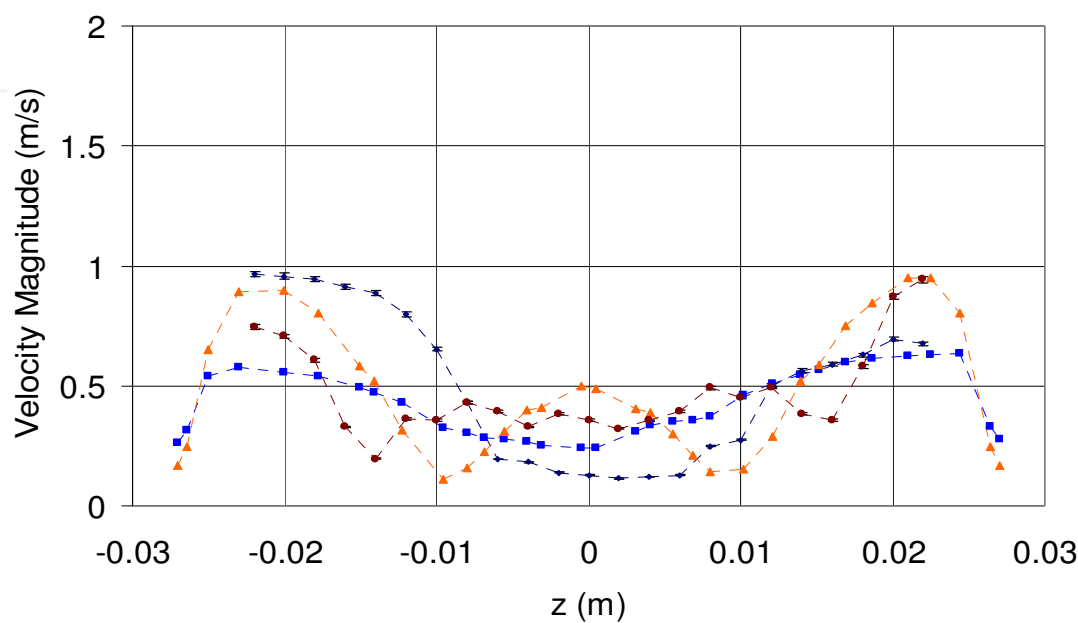
Fig. 12. Velocity on a spanwise slice (x=0.16850 m)
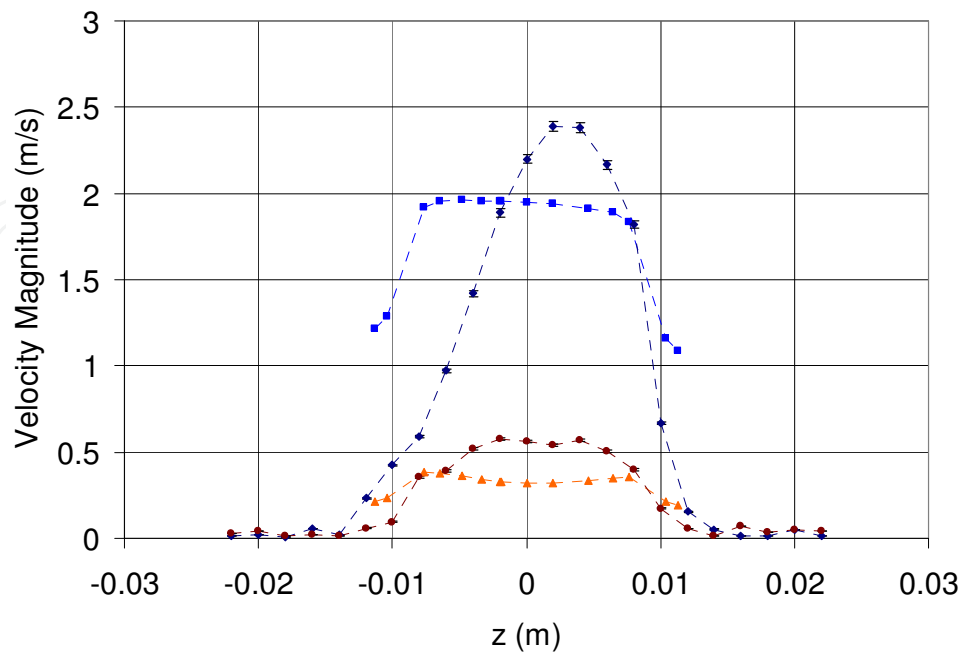
Fig. 13. Velocity on a spanwise slice (x=0.19807 m)
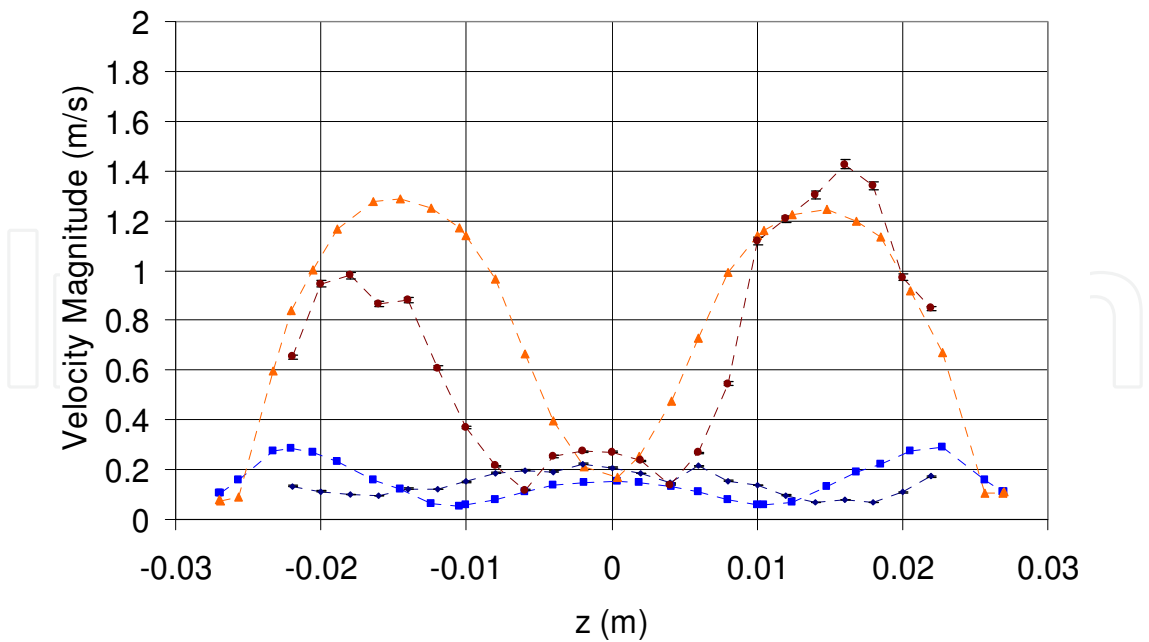
Fig. 14. Velocity on a spanwise slice (x=0.26729 m)

Figure 15 compares the computed and measured turbulence intensity at x=0.19807 m and y=-0.07 m and y=-0.15 m. The values for turbulence intensity are normalized by the maximum velocity magnitude in each data slice. Agreement between computational results and the experimental data is better for the data slice located at the top ⅓ of the plenum, than that at the lower ⅔ of the plenum. The computed turbulence intensity reaches 68% in the lower region of the plenum, approximately 56% higher than the experimentally measured results indicate. This is attributed to the lack of suitable data available to define the turbulence at the inlet.
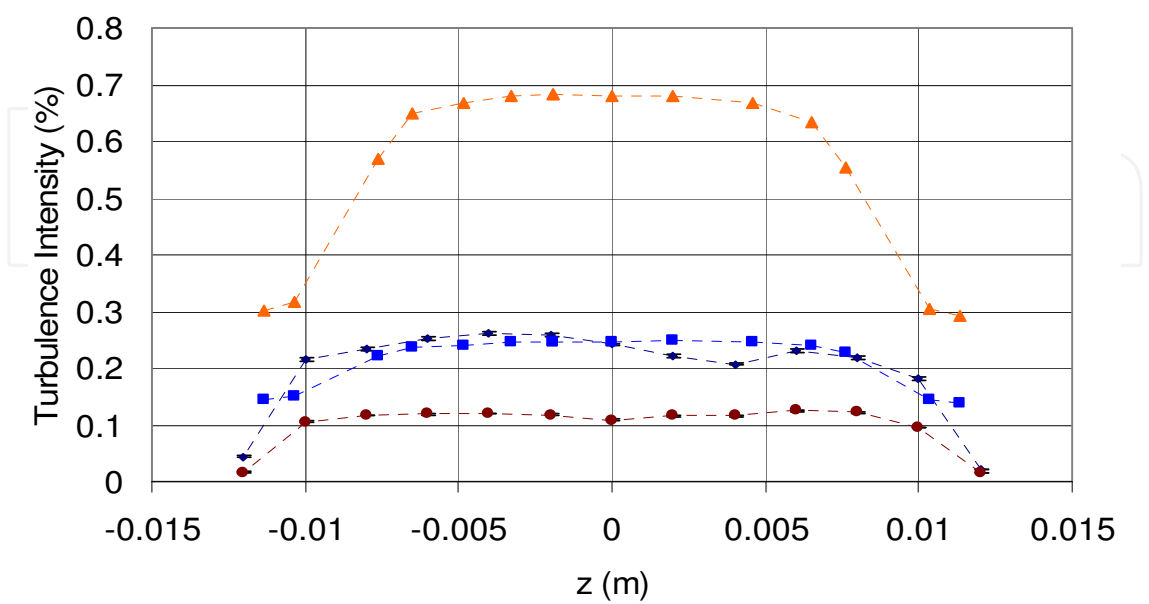
Fig. 15. Turbulence intensity (x=0.19807 m)

3. Gas Cooled Fast Reactor (GFR)

The GFR can be operated at high temperatures, has a high thermal efficiency due to the high temperature of the coolant and, being chemically inert by nature, does not react with the structural materials in the core. Helium is used as the primary coolant. Although water is a much better coolant than helium, it is not appropriate for use in fast breeder reactors due to the neutron thermalization by the light atom hydrogen. Helium has considerable advantages over sodium as a coolant for a fast breeder reactor, especially due to its low interaction with the neutrons and its extremely low chemical activity.

Since GFR cores exhibit high power density and low thermal inertia, the decay heat removal (DHR) in depressurization accidents is a major challenge to be overcome. This is due to the facts that: (1) gases exhibit inherently inferior heat transport properties compared to liquids, and (2) the high surface heat flux of GFR, relative to the high temperature gas-cooled thermal reactor (HTGR), strongly affects the gas flow under natural circulation and places the flow into the mixed convection regime, which is not yet fully understood (Weaver et. al). One of the thermal hydraulic characteristics of GFR is that it is designed for a higher power density than the HTGR by an order of magnitude to achieve good economy. Another characteristic of GFR is its low thermal inertia due to the absence of moderator, such as graphite.

Forced convection refers to flow that is driven by an externally imposed pressure difference. The heat transfer coefficient and friction for such flows strongly depend on the Reynolds number and the Prandtl number. Even in a closed loop where there is a heat source and a heat sink, but no pump or blower to drive the flow, forced convection flow can be achieved by having a large buoyancy head due to a density gradient induced by a temperature difference between the heat source and sink. Natural or free convection, on the other hand, can be defined as the flow that is driven by the local buoyancy force induced by the wall to bulk temperature difference, and the characteristic governing non-dimensional parameters are the Grashof number and Prandtl number (Sabharwall et al. 2009).

Gas coolants at low pressures exhibit poor heat transfer characteristics. This is an area of concern for the passive response targeted by the Generation IV GFR design. For the first 24-hour period, the decay heat removal for the GFR design is dependent on an actively powered blower, which also would reduce the temperature in the fuel during transients, before depending on the passive operation. Natural circulation cooling initiates when the blower is stopped for the final phase of the decay heat removal, as under forced convection the core decay heat is adequately cooled by the running blower. The work done here focuses primarily on the period after the blower has been turned off, as the core is adequately cooled when the blowers are running, thus there was no need to carry out the analysis for the first 24 hours.

3.1 Flow behavior characteristics in the upper plenum of GFR

For natural circulation, the mass flow rate and the corresponding heat removal rate both increase with system pressure. A guard containment structure surrounding the primary system is designed to support an elevated back pressure condition during a depressurization accident. In the GFR, heat is removed by a combination of active and passive systems, and the maximum fuel and core outlet temperatures are maintained within acceptable limits. For the first 24 hours after shutdown when natural circulation alone is not

sufficient to cool the core, the emergency core cooling system (ECCS) operates powered by battery powered blowers. Since the active system provides a relatively large mass flow rate, flow recirculation is unlikely and plume behavior is not considered.

For passive cooling, assessment of the ability of the coolant to flow in the reverse direction or recirculate when the blowers are off requires an understanding of the flow behavior characteristics in the upper plenum. The natural circulation mass flow rate is two orders of magnitude smaller than that for forced circulation allowing significant plume interaction during passive cooling.

3.2 Analysis and modeling procedure

At reduced power and reduced pressure, the mass flow rate of the coolant under natural circulation is much lower than forced circulation (blower flow). This gives rise to the dilemma of decay heat removal of GFR based only on the passive safety system, and makes the understanding of the plume behavior interaction important. In order to understand the interactions between hot plumes in the upper plenum above the core during low flow/low pressure transients, a GFR upper plenum model was generated in GAMBIT and the CFD analysis was carried out in FLUENT (version 6.3.21). The dimensions were provided by the BNL RELAP5 (version 2.4.1.1A) input deck.
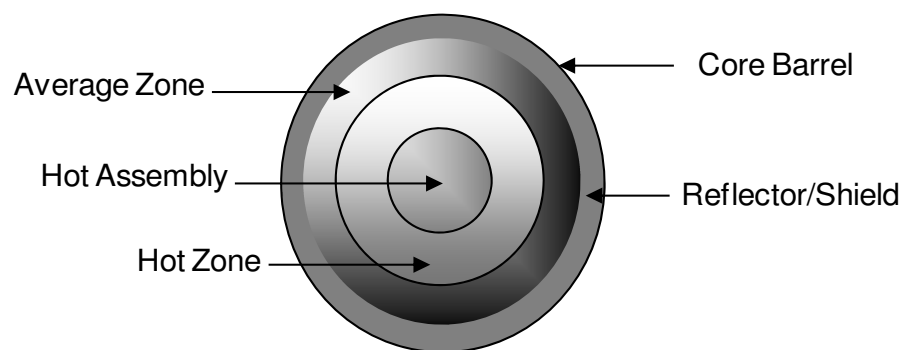

Fig. 16. Horizontal cross-section of GFR core (not to scale)

	Hot Assembly	Hot Zone	Average Zone
Regular Assembly	6	48	303
Control Assembly	0	7	54
Power Fraction (%)	1.7	14.1	84.2
Relative Radial Power Shape	1.31	1.21	0.967

Table 2. Power Distribution in Fuel Zones (Lap et al. 2006)

The RELAP5 model of the fuel in the core is grouped into three radial zones by power (refer Table 2). These radial zones are the hot assembly, the hot zone, and the average zone, as can be seen in the Figure 16. 1.7 % of the power is produced by the hot assembly, 14.1% of the power is produced by the hot zone and the remaining 84.2% is produced by the average zone, here the percentage corresponds to the number of fuel assemblies in that respective radial zone. The 2400 MWt GFR is designed for a system pressure of 7.0 MPa and a core pressure drop of 5.2×10^4 Pa. The primary coolant flow rate is 1249 kg/sec and the core inlet and outlet temperatures are 480 ℃ and 850 ℃, respectively (Lap et al. 2006).

The upper plenum geometry, consisting of a hot assembly, hot zone and average zone, was meshed with GAMBIT. These radial zones acted as the inlet channels to the upper plenum. The gap between the core barrel and the shield along with the gap between the reflector and the shield acted as outlets from the upper plenum. Also included in the model are the power conversion unit (PCU) inlet, which acts as an outlet from the upper plenum and also the lumped PCU (combining the remaining three PCUs together, as four PCUs are required for the 2400 MWt GFR). Piping to the ECCS also acted as an outlet vent from the upper plenum. The inlet mass flow rate and the respective temperature were specified for their corresponding radial zone as inlet boundary conditions, whereas for the outlets, temperatures and pressures were used as the boundary conditions. These values were obtained with the BNL RELAP5 deck. Figure 17 shows the dimensions of the GFR upper plenum, and a 3-D rendering is shown in Figure 18. In GAMBIT, a symmetry boundary condition was applied to reduce the number of mesh nodes and corresponding computational time required to achieve a solution.
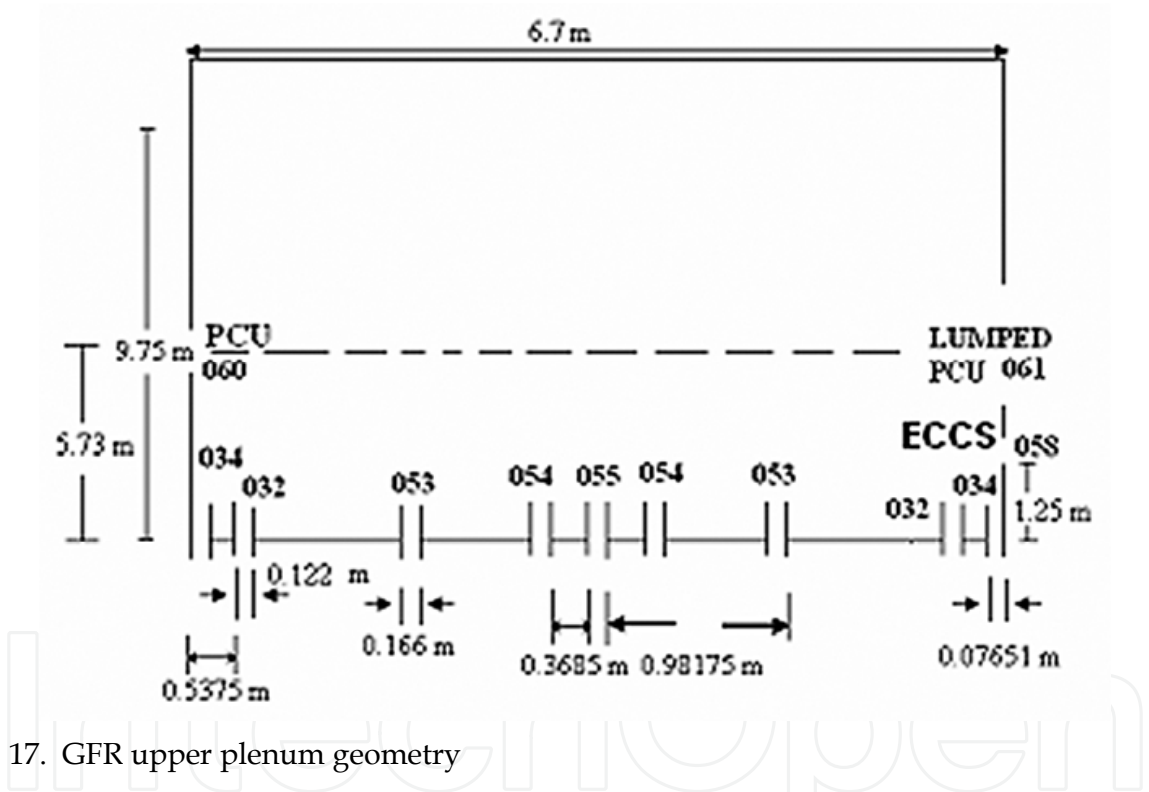

Fig. 17. GFR upper plenum geometry

Label numbers given in Figure 17 are described in greater detail in Table 3.

Volume Number	Component Name	Flow Area (m^2)	Radius (m)	Temperature (K)	Pressure (Pa)	Inlet/Outlet
032	Gap II	0.0154	0.061	762.394	8.00522E+05	Outlet
034	Gap I	0.0103	0.038255	579.794	8.00520E+05	Outlet
053	Average Channel	6.2487	0.083	994.957	8.00524E+05	Inlet
054	Hot Zone	0.9626	0.083	1035.916	8.00524E+05	Inlet
055	Hot Assembly	0.105	0.083	1092.152	8.00524E+05	Inlet
058	ECCS	2.262	0.84834	374.456	8.00473E+05	Outlet
060	PCU	1.606	0.7144	380.697	8.00473E+05	Outlet
061	Lumped PCU	4.818	1.236	376.934	8.00475E+05	Outlet

Table 3. Upper plenum parameters

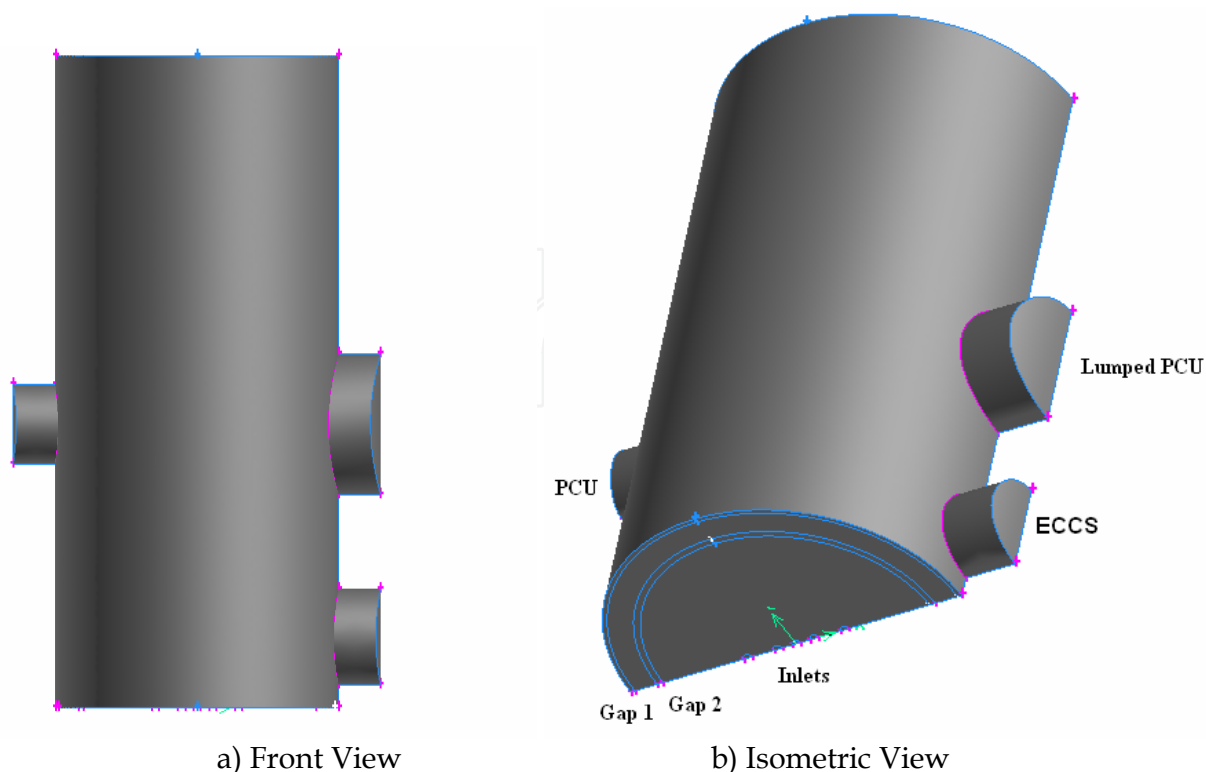a) Front View   b) Isometric View

Fig. 18. Different views of the upper plenum

Inlets

AZ I – First inlet channel in the average zone
AZ II – Second inlet channel in the average zone
HZ I – First inlet channel in the hot zone
HZ II – Second inlet channel in the hot zone
HA –Inlet channel in the hot assembly

Outlets

ECCS – Emergency Core Cooling System
Gap I – Gap between the core barrel and the shield
Gap II – Gap between the reflector and the shield
PCU – Power Conversion Unit

The different views of the upper plenum as shown in Figure 18 were created in the GAMBIT integrated preprocessor for CFD analysis, and then the meshed file was exported to FLUENT for further analyses. In order to understand the plume behavior for the GFR upper plenum, several cases were run, which will be described in detail in the next section. For each case, FLUENT was used to characterize the steady state velocity vectors and corresponding temperature in the upper plenum under passive decay heat removal conditions.

3.3 Modeling results

As described above, several cases were run until the convergence criterion was met. In this case, convergence criteria based upon conservation of energy was set at 1×10^{-6}. In our analyses, the boundary conditions for the inlet and outlet were held constant, as these

numbers were obtained from the BNL RELAP5 deck. These conditions correspond to values of mass flow rate, temperature and pressure 24 hours after the shutdown.

Case	PCU	PCU_Lumped	ECCS	Gap I	Gap II	AZ I	HZ I	HA	AZ II	HZ II
1	X	X	X	0	0	X	X	X	X	X
2	X	X	X	X	X	X	0	X	X	0
3	X	X	X	X	X	0	X	X	0	X
4	X	X	X	X	X	X	X	0	X	X

Table 4. Different cases for the analyses

In Table 4, the X corresponds to "on" (coolant is flowing) and 0 corresponds to "off" (no flow). For all the cases, convergence criteria were met, both for steady and unsteady state. Conservation of mass was verified for all cases, as can be seen in Table 5.

Case	PCU	PCU_Lumped	ECCS	Gap I	Gap II	AZ I	HZ I	HA	AZ II	HZ II	$\delta m_{in} - \delta m_{out}$
1	-0.754	-4.573	-2.184	0	0	1.525	1.5	1.47	1.525	1.5	0.00935891
2	-0.411	-6.884	-1.927	1.975	2.721	1.525	0	1.47	1.525	0	-0.0049226
3	-0.138	-0.606	-3.26	-0.327	-0.054	0	1.5	1.47	0	1.5	0.08266951
4	-0.026	-3.12	-3.022	0.019	0.19	1.525	1.5	0	1.525	1.5	0.09210049

Table 5. Mass flow rate (kg/sec) for all the cases[1]

Case 1

In case 1, the gap between the core barrel and the shield along with the gap between the shield and the reflector were closed. The convergence criteria were met as can be seen from Figure 19. The largest flow rate was through the lumped PCU opening, as expected.

All the velocity vectors are at nearly the same temperature, since no flow is allowed through the gaps, which makes all the plumes rise. Thus, colder plumes come into contact with the hotter plumes and attain the same temperature before leaving through other outlets.

Case 2

In this case, two inlets (hot zones) are closed. Gaps located close to the average zone inlet have a net positive mass flow rate because the flow rate of the average zone is so high that it entrains the plumes entering the gaps with it and thus makes the gaps behave like an inlet. In this case, the maximum flow is out through the lumped PCU, as expected.

Case 3

In this case, the average zone inlets are closed and the gaps act as an outlet unlike in case 2, thus proving the validity of the reasoning for case 2. The maximum amount of flow in this case is into the ECCS. Most of the flow exits the ECCS because the average zone inlet channels are closed. Thus, plumes near that location are comparatively cold, and do not have enough momentum to flow upwards towards the lumped PCU.

---

[1] Positive values indicate flow into the plenum, whereas negative values indicate flow out of the plenum.

Case 4

In this case, the hot assembly inlet is closed. Since the average zone inlet is open, the gaps act as an inlet, similar to case 2. Both the ECCS and lumped PCU have almost the same amount of flow leaving from the upper plenum.

Plumes near the hot assembly exhibit colder temperatures and thus move towards the ECCS, whereas the plumes near the hot zone and average zone travel towards the lumped PCU.
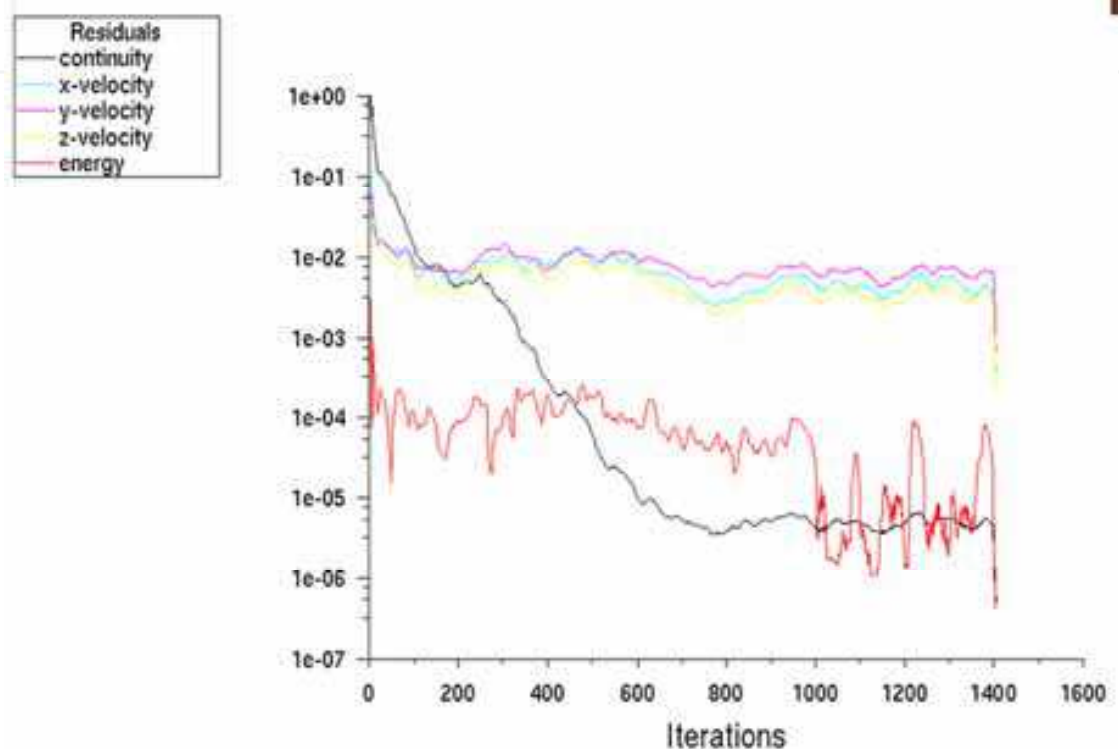

Fig. 19. Residual plot for convergence (Case 1)

3.4 Discussion

In all the cases investigated, as can be seen from Table 5, the net mass flow in the upper plenum is not equal to zero, because in an unsteady problem some amount of mass gets accumulated in the plenum, but the magnitude of the net mass flow was small enough to let us believe that mass was being conserved (or the problem was in steady state). The positive magnitude of the mass flow rate refers to the incoming flow whereas the negative magnitude of the mass flow rate refers to the outgoing flow. In all the cases the recirculation patterns of plumes were observed in the top of the upper plenum.

If the mesh is refined, then the net mass flow rate through the upper plenum could be further reduced and thus more precise values for the outlet mass flow rate could be obtained. The analysis done here indicates that the recirculation pattern and the outlet flow depend upon which inlet channels are open, such as in case 2 when the average channel was off. Both gaps behave as outlets and aid in the decay heat removal, whereas in the other cases there is no flow in those gaps, which in an actual system is similar to a flow stagnation, which can cause cracks to develop, and also lead to generation of hot spots in the core. To

more fully capture the plume interaction behavior, this analysis should be performed with a finer mesh and with other coolants and mixtures. This phenomenon may be important if blower power is lost. The analyses should also be carried out with CO_2 for comparison with helium. CO_2 is denser than helium and is thus a better natural convection coolant.

In an accident scenario, if air ingresses inside the vessel, air and helium can mix, which can have a detrimental effect on the helium plume rising in the upper plenum. The initial vertical velocity of the plume is soon greatly reduced, upon encountering the air. If at the same time forced flow is not available, flow reversal in some of the inlet channels could result.

3.5 Comparative study

In order to understand the plume behavior for the GFR upper plenum, a few different cases were run, with air, helium (Table 6) and helium-air mixture (Table 7). For each case, FLUENT was used to characterize the steady-state velocity vectors and corresponding temperature in the upper plenum under passive decay heat removal conditions. In the previous sections explanations have been provided for air as the coolant. In this section, the behavior air is compared to other coolants. In the case of helium-air mixture, maximum flow was through the lumped PCU, similar to that of the air, but with helium, maximum flow was through the ECCS, for case 1. For case 2, the maximum flow was through the gap I for the helium-air mixture, whereas maximum flow was observed through the lumped PCU for air and helium. For case 3 maximum flow was observed through the lumped PCU for both helium-air mixture and helium, whereas for air, the maximum flow was through ECCS. For case 4, maximum flow was observed through the lumped PCU for air and helium, whereas in the case of the mixture of helium and air, maximum flow was observed through gap1. The analysis done here indicates that the recirculation pattern and the outlet flow is dependent on which inlet channels are open and also indicate dependence of the mass flow on the type of the coolant, i.e., for the same conditions the behavior of plumes was observed to be different, which should be significant for the study of flow characteristics in the upper plenum during low flow/low pressure transients.

Case	PCU	PCU_Lumped	ECCS	Gap I	Gap II	AZ I	HZ I	HA	AZ II	HZ II	$\delta m_{in}-\delta m_{out}$
1	38.88	-5.676	-47	0	0	1.526	1.5	1.47	1.525	1.5	-5.96159
2	0.045	-5.8	-4.6	2.027	2.888	1.526	0	1.47	1.525	0	-0.95866
3	-0.46	-5.848	-4	2.187	3.693	0	1.5	1.47	0	1.5	-0.0062
4	-0.9	-5.981	-1.5	0.729	1.586	1.526	1.5	0	1.525	1.5	-0.00664

Table 6. Mass flow rate (kg/sec) for all the cases (helium)

Case	PCU	PCU_Lumped	ECCS	Gap I	Gap II	AZ I	HZ I	HA	AZ II	HZ II	$\delta m_{in}-\delta m_{out}$
1	-0.754	-4.573	-2.185	0	0	1.526	1.5	1.5	1.53	1.5	0.009359
2	-0.254	-1.178	0.062	-1.859	-1.517	1.526	0	1.5	1.53	0	-0.225347
3	-0.113	-2.203	-0.077	-1.254	-0.515	0	1.5	1.5	0	1.5	0.307385
4	-0.122	-0.63	-0.209	-2.811	-2.583	1.526	1.5	0	1.53	1.5	-0.303515

Table 7. Mass flow rate (kg/sec) for all the cases (helium and air)

4. Summary and recommendations

This section summarizes the major results of the VHTR and GFR CFD studies and provides recommendations for further work.

4.1 Recommendations from VHTR study

FLUENT converged more readily with the polyhedral grid than with the unstructured grid. The VHTR results presented in this paper were obtained using the "super-fine" polyhedral grid. Results obtained using the polyhedral grid more closely matched the experimental data than the results obtained using the unstructured grid, although the agreement was still far from optimal. Since the inlet boundary condition was not matched exactly, differences between the computed and measured results are expected. However, the large percentage difference in the computed mean velocity between the grids used in this study indicates that additional grid studies are needed. For future studies, computations should be performed on an even more refined grid until the results do not change between subsequent grids. In this study, the computational grids became unwieldy and the solutions required long execution times when the number of grid points was increased beyond that of the "super-fine" grid.

Three-dimensional CFD predictions of flow through a complex geometry representing the lower plenum of an advanced reactor have been performed and compared with laboratory measurements obtained for a scaled model. The major trends seen in the experimental data are captured by the CFD results. The computed versus experimental results are in general agreement, but the quantitative agreement could be improved. Again, it is stressed that the purpose of this work is to better define improvements that can be made to the next set of computations and experiments. Better agreement between the computed and measured results could be achieved by modifying both the computational model and the laboratory setup. Discrepancies can be attributed to features of the current experimental setup and computational model.

Wall and thermal effects

Wall effects on mixing in a confined channel are likely to cause significant differences between the actual lower plenum flow and that of the flow test model. The incorporation of thermal effects will also have a significant impact on the flow in this region. These effects must be accurately described in order to produce the necessary data for licensing and safety analysis of these advanced concept reactors.

Data acquisition – time resolution

The time-averaging procedure used by the computational code averages the results obtained at every time-step (approximately 0.01 sec), whereas the experimental setup averages the data measured at much larger time intervals (0.1 sec). To obtain sufficient data points to capture the flow unsteadiness, the data acquisition system should have the ability to capture data with sufficient resolution (i.e., >200 Hz). A high-speed PIV system could provide this data.

Data acquisition – spatial resolution

Due to the fact that the PIV method employed is not accurate near the jet walls, the data in near-wall region was missing. The profiles were also very coarse – in some locations there

were only eight data points representing the velocity profile at a given location across the jet. Thus, when integrated the velocity profiles under-predicted the mass flow rate. To conserve mass in the plenum, a mass flow rate boundary condition was used, which employed a constant velocity across the inlet jet. Future studies should provide for the acquisition of adequate velocity and turbulent kinetic energy inlet profiles for use as boundary conditions to the computations. A different approach to obtain data at the inlet jets should be considered. Perhaps complementing PIV with laser Doppler velocimetry (LDV) could provide velocity data that, when integrated, yields the correct mass flow rates. LDV can resolve velocities in the proximity of the wall to about y+<1, which is more precise than PIV but much more time-intensive. The uncertainty in PIV is about 0.3 pixels. LDV uses much smaller control volumes.

Turbulence modeling

To accurately capture and represent turbulent mixing is a considerable experimental, theoretical and computational challenge (Dimotakis, 2005). Research by von Lavante and Laurien (Lavante and Laurien, 2007) shows that the k-ε turbulence model performs poorly for flows with strong streamline curvature, since the generation and dissipation of turbulence is anisotropic for these flows. For their application, two-equation turbulence models were found to be too dissipative and as a consequence rapidly dissipate the vorticity present in mixing regions. It is anticipated that the Reynolds Stress Model (RSM) would perform significantly better than the k-ε model when strong recirculation zones and eddies are present. For the lower plenum flow, the use of the RSM should be explored and the results compared with those obtained using the k-ε turbulence model.

4.2 Recommendations from GFR study

The GFR flow within the upper plenum was characterized during natural circulation 24 hours after a loss of coolant accident. In future work, the same analyses should be carried out for mixtures of different gases such as helium and carbon dioxide (CO_2), and also CO_2 and air. In all the cases, investigated here, the net mass flow in the upper plenum is not equal to zero, because in an unsteady problem some amount of mass is accumulated, but the magnitude of the net mass flow was small enough to assume that problem was in steady state. The positive magnitude of the mass flow rate refers to the incoming flow whereas the negative magnitude of the mass flow rate refers to the outgoing flow. In all the cases a recirculation pattern of plumes was observed at the top of the upper plenum. Performing the analyses with different coolants and using a finer mesh will lead to an improved understanding of the plume behavior in the upper plenum at low flow and low pressure conditions.

4.3 Acknowledgements

favoring by the U.S. Government, any agency thereof, or any company affiliated with Idaho National Laboratory.

5. References

Celik, I. B. (2006). Procedure for Estimation and Reporting of Discretization Error in CFD Applications, Mechanical and Aerospace Engineering Department, West Virginia University.

Celik, I.B. (i) (2006). Overview of Turbulence Modeling for Industrial Applications, Mechanical and Aerospace Engineering Department, West Virginia University.

Cheng, L.Y., Ludewig, H., and Jo, J. (2006). Emergency Decay Heat Removal in a Gen-IV Gas-Cooled Fast Reactor, *14th International Conference on Nuclear Engineering*, ICONE14-89681, Florida.

Condie, K.G., G. E. McCreery, H. M. McIlroy Jr., and D. M. McEligot (2005). Development of an Experiment for Measuring Flow Phenomena Occurring in a Lower Plenum for VHTR CFD Assessment, INL/EXT-05-00603, Idaho National Laboratory, September 2005.

Dimotakis, P. E. (2005). Turbulent Mixing, *Annual Review of Fluid Mechanics*, Vol. 37, pp. 329–356.

FLUENT (2007). FLUENT Inc.: Lebanon, NH, 03766.

General Atomics (1996). *Gas Turbine – Modular Helium Reactor (GT–MHR) Conceptual Design Description Report*, General Atomics 910720, Rev. 1, July 1996.

Johnson, R. W., Guillen, D.P., and Gallaway, T. (2006). *Investigations of the Application of CFD to Flow Expected in the Lower Plenum of the Prismatic VHTR*, INL/EXT-06-11756, September 2006.

Johnson, R.W. (2006). Modeling Strategies for Unsteady Turbulent Flows in the Lower Plenum of the VHTR, *CFD4NRS Workshop on Benchmarking of CFD Codes for Application to Nuclear Reactor Safety*, Garching, Munich, Germany.

McIlroy, H. M., McEligot, D.M., Schultz, R.R., Christensen, D., Pink, R.J., and Johnson R.C. (2006). *PIV Experiments to Measure Flow Phenomena in a Scaled Model of a VHTR Lower Plenum*, INL/EXT-08-15161, September 2006.

Nuclear Energy Institute (2008). *Nuclear Energy: Just the Facts*, 1776 I St., NW, Washington, DC, 20006, www.nei.org.

O'Brien, J.E., Stoots, C.M., Herring, J.S., and Harvigsen, J.J. (2007). Performance of Planar High-Temperature Electrolysis Stacks for Hydrogen Production from Nuclear Energy, *Nuclear Technology*, Vol. 158, p. 118-131.

Sabharwall, P., Utgikar, V., and Gunnerson, F. (2009). Dimensionless Numbers in Boiling Fluid Flow for Thermosyphon and Heat Pipe Heat Exchangers, *Journal of Nuclear Technology*, Vol. 167, August 2009.

Schultz, R.R., et al. (2006). Specifying Standard Problems for Validating Advanced Reactor Computational Fluid Dynamics Analysis Tools, *American Nuclear Society Transactions*, Vol. 95, p. 836-837.

Smith, B.L., Stepan, J.J., and McEligot, D.M. (2006). Velocity and Pressure Measurements Along a Row of Confined Cylinders, *2006 ASME Fluids Engineering Summer Conference*, Miami, FL: Proceedings of ASME-FED.

U.S. Energy Information Administration, *Annual Energy Outlook,* 2011.

Weaver, K., et al., Gas-Cooled Fast Reactor (GFR) *FY05 Annual Report*, Idaho National Laboratory Report INL/EXT-05-00799, September 2005.
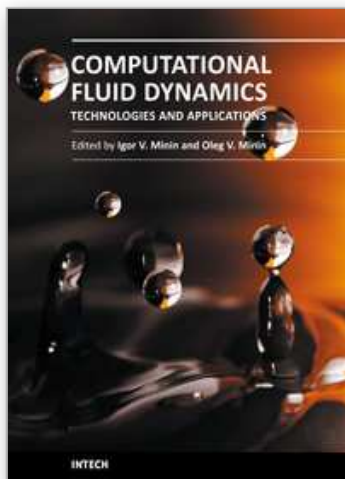
Computational Fluid Dynamics Technologies and Applications

Edited by Prof. Igor Minin

This book is planned to publish with an objective to provide a state-of-art reference book in the area of computational fluid dynamics for CFD engineers, scientists, applied physicists and post-graduate students. Also the aim of the book is the continuous and timely dissemination of new and innovative CFD research and developments. This reference book is a collection of 14 chapters characterized in 4 parts: modern principles of CFD, CFD in physics, industrial and in castle. This book provides a comprehensive overview of the computational experiment technology, numerical simulation of the hydrodynamics and heat transfer processes in a two dimensional gas, application of lattice Boltzmann method in heat transfer and fluid flow, etc. Several interesting applications area are also discusses in the book like underwater vehicle propeller, the flow behavior in gas-cooled nuclear reactors, simulation odour dispersion around windbreaks and so on.

How to reference

In order to correctly reference this scholarly work, feel free to copy and paste the following:

INTECH
open science | open minds